View Article Online
View Journal

Dalton Transactions

An international journal of inorganic chemistry

Accepted Manuscript

This article can be cited before page numbers have been issued, to do this please use: A. Bhanja, S. Roy Chaudhuri, A. B. Tsanai, S. P. Vyas, F. Ortu, L. Smythe, M. Murrie, R. Goswami and D. Ray, *Dalton Trans.*, 2023, DOI: 10.1039/D2DT03932J.

ROYAL SOCIETY OF CHEMISTRY

rsc.li/dalton

View Article Online
DOI: 10.1039/D2DT03932J

ARTICLE

Synthesis and characterization of two self-assembled $[Cu_6Gd_3]$ and $[Cu_5Dy_2]$ complexes exhibiting magnetocaloric effect, slow relaxation of magnetization and anticancer activity

fReceived 00th January 20xx,
Accepted 00th January 20xx

DOI: 10.1039/x0xx00000x

Avik Bhanja,[a] Sangeeta Roy Chaudhuri,[a] Angelos B. Canaj,[b] Shachi Pranjal Vyas,[c] Fabrizio Ortu,[d] Lucy Smythe,[b] Mark Murrie,[b] Ritobrata Goswami[c] and Debashis Ray*[,a]

Two new paths for coordination driven self-assembly reactions under the binding supports of 2-((1-hydroxy-2-methylpropan-2-ylimino)methyl)-6-methoxyphenol (H_2L) have been discovered from reactions of $Cu(ClO_4)_2{\cdot}6H_2O$, NEt_3 and $GdCl_3/DyCl_3{\cdot}6H_2O$ in $MeOH/CHCl_3$ (2:1) medium. Similar synthetic protocol is useful to provide two different types of self-aggregated molecular cluster in $[Cu_6Gd_3(L)_3(HL)_3(\mu_3\text{-}Cl)_3(\mu_3\text{-}OH)_6(OH)_2]ClO_4{\cdot}4H_2O$ (**1**) and $[Cu_5Dy_2(L)_2(HL)_2(\mu\text{-}Cl)_2(\mu_3\text{-}OH)_4(ClO_4)_2(H_2O)_6](ClO_4)_2{\cdot}2NHEt_3Cl{\cdot}21H_2O$ (**2**). Adopted reaction procedure established the importance of the HO^- and Cl^- ions for the mineral-like growth of the complexes, derived from solvent and metal ion salts. In case of complex **1**, one Gd^{III} center has been trapped at the central position of the core upheld by six μ_3-OH and three μ_3-Cl groups whereas for complex **2** one Cu^{II} center was trapped using four μ_3-hydroxo and two μ-chlorido groups. The magnetothermal behavior of **1** has been examined for a magnetocaloric effect of $-\Delta S_m$ = 11.3 J kg^{-1} K^{-1} at 2 K for ΔH = 7 T. Whereas the magnetic susceptibility measurements of **2** showed slow magnetic relaxation with U_{eff} = 15.8 K and τ_0 = 9.8 x 10^{-7} s in zero external dc field. Cancer cell growth inhibition studies proved the potential of both the complexes with interestingly most activity for Cu_6Gd_3 complex against human lung cancer cells. Both complexes **1** and **2** also exhibited DNA and human serum albumin (HSA) binding aptitudes in relation to the involved binding sites and thermodynamics.

Introduction

In recent years coordination driven mineralization processes have been enthusiastically examined for the synthesis of novel molecular magnetic materials,[1–6] incorporating both *3d* and *4f* ions in varying numbers, showing importance of small anionic linkers for the overall growth. Studies on these *3d-4f* complexes, shows promising results in understanding their electronic structures, vibrations, and spin dynamics relevant to detail magnetic behaviour including quantum information processing and quantum computing.[7–10] Manipulation within the metallo-supramolecular domain and tuning of the role of individual metal ions in self-assembly of 3d and 4f ions would thus be exciting. In this endeavour, the choices for metal ion salts are extremely vital for a particular type of product, because of their differing Lewis acidity. Molecule based magnetic materials, known as single-molecule magnets (SMMs), are molecular species that retain their magnetization in the absence of an applied field[11–13] and they can block magnetisation involving an energy barrier (U_{eff}) to result magnetic hysteresis of molecular origin.[14–16] Potential applications of these SMMs will necessitate not only the ability to function at higher temperatures, but also to be chemically robust in air and high moisture level. The recent attention in molecular aggregates involving multiple numbers of Cu^{II} and Ln^{III} ions has been developed from the collective ability of these metal ions in stabilizing multinuclear structures of unprecedented type through the involvement of several coordinating and bridging oxygen donors.[17–21] These aggregates are often known to show interesting magnetic behaviour.[22–24] Incorporation of Dy^{III} in molecular aggregates generates a strong axial magnetic anisotropy for the complexes showing significant energy barriers and high blocking temperatures.[25–29] On the other hand, it has been observed that $Cu^{II}\cdots Gd^{III}$ compounds usually shows weak ferromagnetic exchange interactions and display appreciable magnetocaloric effect (MCE) (Table S1).[30–31]

Apart from the use of lanthanide(III) ions and their complexes as molecular magnet, lanthanide ions are good candidate for applications as probes for bioassays because of their higher charge-to-radius ratio in comparison to other biological Lewis acids such as Ca^{II}, Mg^{II} and because of their flexible coordination geometry.[32] Lanthanide ions are

[a.] Department of Chemistry, Indian Institute of Technology, Kharagpur 721302, India
[b.] School of Chemistry, University of Glasgow, University Avenue, Glasgow, G12 8QQ, UK
[c.] School of Bioscience, Indian Institute of Technology, Kharagpur 721302, India
[d.] School of Chemistry, University of Leicester, LE1 7RH Leicester, UK

†Electronic Supplementary Information (ESI) available: SHAPE analysis, Crystal data, PXRD curves, selected bond lengths and angles, Mass spectra, magnetization plots, cytotoxicity, DNA and protein binding studies are described in Fig. S1–S20 and Tables S1–S13 in the text. CCDC 2184365 and 2184368 contain the supplementary crystallographic data for this paper. See DOI: 10.1039/x0xx00000x

efficiently utilized for different medical applications such as magnetic resonance imaging (MRI) contrast agents, for palliative care in patients suffering with osteosarcoma and as fluorescent probes in cell studies.[33] Combination of biologically relevant ligands with lanthanide(III) ions is one of the effective strategies for designing anticancer drug. Recently many studies reported that a series of lanthanide(III) complexes bearing bioactive ligands which displayed enhanced *in vitro* and *in vivo* anticancer activity.[34] Schiff bases are important functional ligands in pharmacological applications such as antimicrobial, antitubercular, analgesic and antitumor activities.[35–38] Ligands with ONO binding sites and aroylhydrazone skeleton can be associated with Ln^{III} ions to obtain various target compounds which can interact with biomacromolecules like DNA and HSA.[39]

Phenol function bearing ligands containing coordinating N donor from imine group and O donors from phenol, alcohol and ether groups can be the most useful and versatile bridging agent to construct *3d-4f* ion-based coordination clusters.[40–43] Wherein the N atom can be utilized to trap the *3d* ions selectively and the O atom is more inclined to bind the *4f* ions in accordance with the SHAB principle. We were engaged in the synthetic exploration of the self-assembled versions of the reaction products resulting from the Schiff base anions and chosen *3d* and *4f* ions. Earlier we have used 2-amino-2-methylpropan-1-ol as amine alcohol Schiff base tail for synthesizing the Mn_3 and Mn_4 aggregates.[44] Herein we explored the stepwise reaction potential of $Cu(ClO_4)_2{\cdot}6H_2O$ and $GdCl_3/DyCl_3{\cdot}6H_2O$ and NEt_3 for deprotonation toward the ligand 2-((1-hydroxy-2-methylpropan-2-ylimino)methyl)-6-methoxyphenol (H_2L; Chart S1 in the ESI) in MeOH-$CHCl_3$ solvent mixture in 2:1 v/v. The attempted reactions gave coordination aggregates $[Cu_6Gd_3(L)_3(HL)_3(\mu_3\text{-}Cl)_3(\mu_3\text{-}OH)_6(OH)_2]ClO_4{\cdot}4H_2O$ (**1**) and $[Cu_5Dy_2(L)_2(HL)_2(\mu\text{-}Cl)_2(\mu_3\text{-}OH)_4(ClO_4)_2(H_2O)_6](ClO_4)_2{\cdot}2NHEt_3Cl{\cdot}21H_2O$ (**2**). The characterization program for these two structurally different assemblages includes identification of molecular magnet types with respect to magnetic relaxation and magnetothermal behaviors. Moreover, the importance of different lanthanide ion complexes as bio probes has been established by comparing the cytotoxicity and DNA/HSA binding study of both the complexes.

Result and Discussion

Synthetic protocol

The reaction between 2-amino-2-methylpropan-1-ol and 2-hydroxy-3-mehoxybenzaldehyde in refluxing condition using MeOH as solvent provided yellow oily mass of H_2L. Similar Schiff base ligands with alcohol arm were found to be effective to incorporate *3d* and *4f* ions side by side, where imine N donor shows preferential binding of *3d* ion and has pinning of lanthanide ion by two adjacent O donors.[45] Such type of ligands developed on 2-amino-2-methylpropan-1-ol, has been used to obtain homometallic clusters of {Ni_4 and Ni_6}[46], {Mn_3

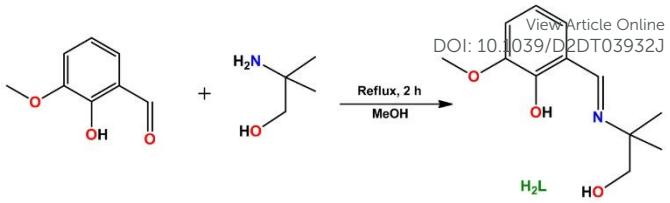

Scheme 1 Schiff base condensation for H_2L

and Mn_4}[44], {Mn_6}[47] from our laboratory. Several other examples of similar Schiff base ligands are known to produce [Cu_4] clusters having cubane,[48] step–cubane[49] or open–cubane[50] topology. These interesting results motivate us to synthesize *o*-methoxo substituted ligand H_2L according to scheme 1 and then explore the reactivity of this ligand to prepare high nuclearity 3d–4f complexes using $LnCl_3{\cdot}6H_2O$ and $Cu(ClO_4)_2{\cdot}6H_2O$ salts. Through several attempts, we have been successful in getting the corresponding Gd^{III} and Dy^{III} complexes. Report of synthesis of Tb^{III}, Ho^{III}, La^{III} or Y^{III} analogues in this paper were not possible as we are not able to synthesize single crystals of the respective compounds. The development of reaction protocol and isolation of single crystals of **1** and **2** are dependent on the choice of solvent mixture as MeOH-$CHCl_3$ (2:1 v/v ratio), amount of base for deprotonation and the molar ratio of the reactants.

The stepwise additions of H_2L, $Cu(ClO_4)_2{\cdot}6H_2O$, $LnCl_3{\cdot}6H_2O$ (Ln = Gd^{III}, **1**; Dy^{III}, **2**) and NEt_3 in 1:1:0.5:2 molar ratio in MeOH-$CHCl_3$ (2:1, v/v) medium under stirring condition afforded a bluish green solution from which block shaped green crystals of **1** and **2** appeared after a week by controlled evaporation of the reaction mixture. Elemental analysis and X-ray structure determination confirmed the molecular formula of complex **1** as $[Cu_6Gd_3(L)_3(HL)_3(\mu_3\text{-}Cl)_3(\mu_3\text{-}OH)_6(OH)_2]ClO_4{\cdot}4H_2O$. The coordination aggregation of nine metal ions of two different types is achieved from coordination capping of six ligand backbone followed by support from six μ_3-hydroxido and three μ_3-chlorido bridges finally provided complex **1** as summarized in eqn 1.

$$3GdCl_3{\cdot}6H_2O + 6Cu(ClO_4)_2{\cdot}6H_2O + 6H_2L \longrightarrow [Cu_6Gd_3(L)_3(HL)_3(\mu_3\text{-}Cl)_3(\mu_3\text{-}OH)_6(OH)_2]ClO_4{\cdot}4H_2O + 11ClO_4^- + 6Cl^- + 17H^+ + 42H_2O \quad \ldots(1)$$

In contrast use of $DyCl_3{\cdot}6H_2O$ in lieu of $GdCl_3{\cdot}6H_2O$ followed a completely different aggregation path for a new type of heptanuclear *3d-4f* complex. In presence of the Dy^{III} salt, the self-assembly path took the help of four ligand anions, four μ_3-hydroxido and two μ-chlorido bridging to grow the heptanuclear aggregate $[Cu_5Dy_2(L)_2(HL)_2(\mu\text{-}Cl)_2(\mu_3\text{-}OH)_4(H_2O)_6(ClO_4)_2](ClO_4)_2{\cdot}2NHEt_3Cl{\cdot}21H_2O$. The aggregation reaction for **2** is summarized in eqn 2.

$$2DyCl_3{\cdot}6H_2O + 5Cu(ClO_4)_2{\cdot}6H_2O + 4H_2L + 2NEt_3 \longrightarrow [Cu_5Dy_2(L)_2(HL)_2(\mu\text{-}Cl)_2(\mu_3\text{-}OH)_4(H_2O)_6(ClO_4)_2](ClO_4)_2{\cdot}2NHEt_3Cl{\cdot}21H_2O + 6ClO_4^- + 2Cl^- + 8H^+ + 11H_2O \quad \ldots(2)$$

View Article Online
DOI: 10.1039/D2DT03932J

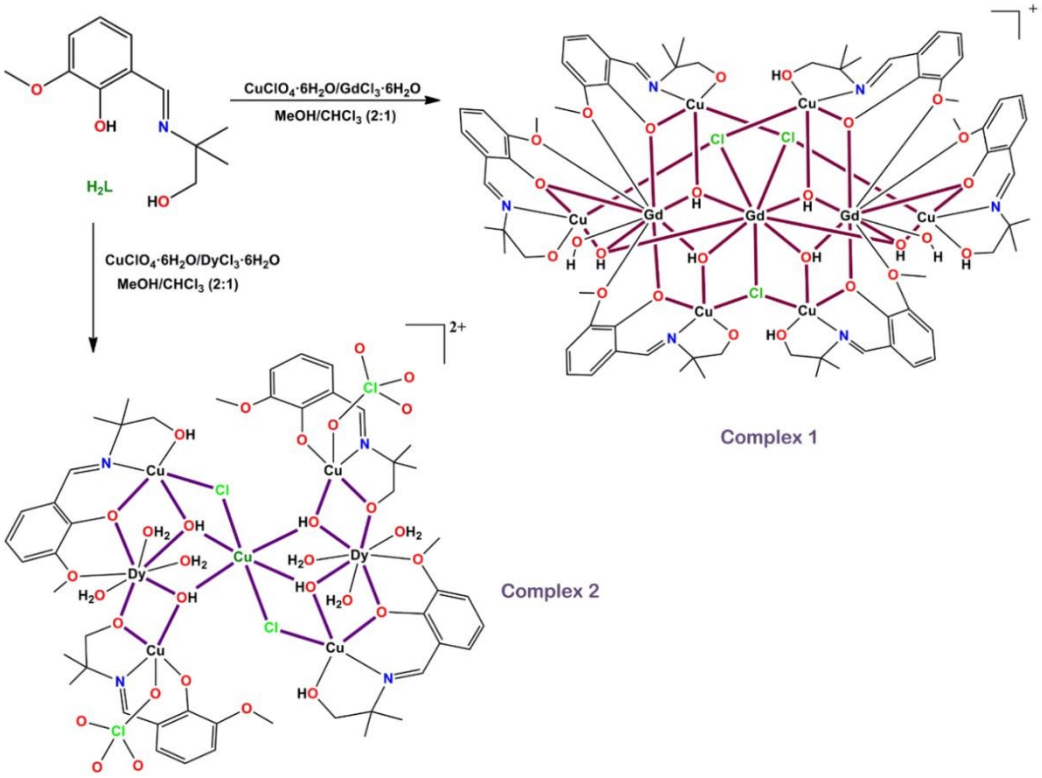

Scheme 2 Synthetic routes for **1** and **2**

Both the complexes were characterized and analysed by PXRD and FT-IR spectroscopic measurements. The powder pattern of the experimental and the simulated PXRD plot of both the samples match well, which justifies the phase purity of the bulk compounds (Fig. S1 in the ESI). The FTIR spectra of **1** and **2** in solid form have characteristic signatures in the fingerprint region. The identification of Cu^{II}–N_{imine} bonds were clearly discernible in from the characteristic $\bar{\nu}_{C=N}$ band at 1634 cm^{-1} for **1** and 1644 cm^{-1} for **2**, for free ligand the band appeared at 1631 cm^{-1} (Fig. S2 in the ESI). The presence of two different types of perchlorate anions have been confirmed from the respective stretches. The crystal lattice trapped ClO_4^- ions in T_d symmetry showed strong bands at ~1077 cm^{-1} and ~1090 cm^{-1} for $\nu_3(T_2)(\nu_{ClO})$ mode and a medium intense ones at 621 and 625 cm^{-1} for $\nu_4(T_2)(\delta_{dOClO})$ vibration modes for **1** and **2** respectively.[51] For complex **2**, the monodentate coordination of ClO_4^- ion in C_{3v} symmetry splits the ν_3 and ν_4 modes into three and two components respectively. The peaks were obtained at 1090, 1102 and 1141 cm^{-1} for ν_3 mode and at 625 and 636 cm^{-1} for ν_4 mode.

Crystal structure description of 1

Single crystals of complex **1** were obtained after four days from the reaction mixture in MeOH-$CHCl_3$. The complex crystalizes in monoclinic $P2_1/c$ space group and the molecular structure was identified as $[Cu_6Gd_3(L)_3(HL)_3(\mu_3\text{-}Cl)_3(\mu_3\text{-}OH)_6(OH)_2]ClO_4{\cdot}4H_2O$ (Fig. 1). The unit cell of **1** consists of two Cu_6Gd_3 units, eight lattice water molecules and two perchlorate anions. The crystal structure determination parameters are collected in Table S2 and the selected bond length and angles are presented in Tables S8–S9 of the ESI.

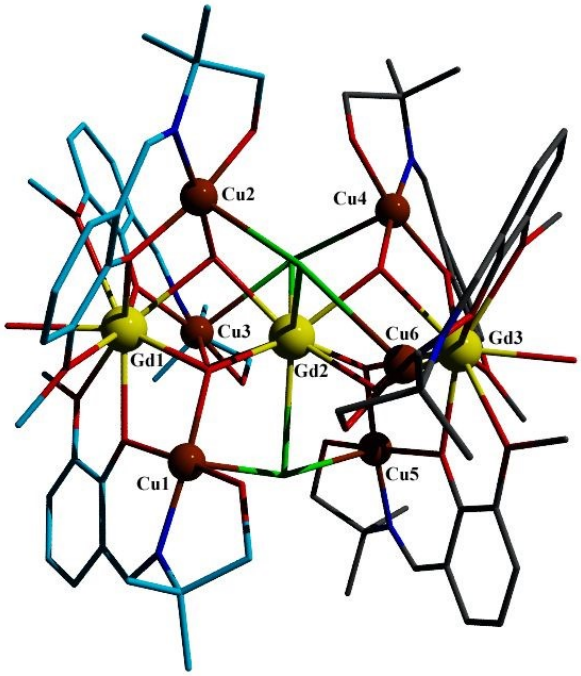

Fig. 1 Molecular structure of **1**. Hydrogen atoms, solvent molecules and counter anions are omitted for clarity. Colour code: Cu, brown; Gd, yellow; C, grey and cyan; O, red; N, blue; Cl, green.

View Article Online
DOI: 10.1039/D2DT03731

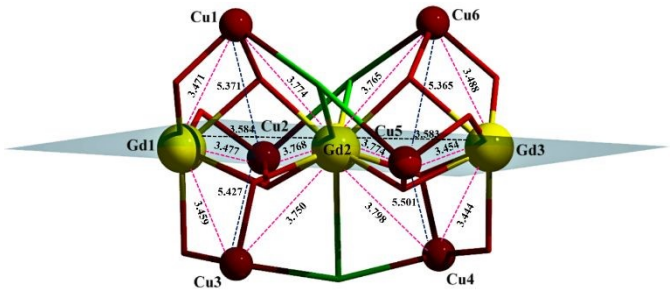

Fig. 2 Mean plane of **1** (grey in colour) hosting Gd^{III} centers showing Cu···Cu, Cu···Gd and Gd···Gd separations in Å. Colour code: Cu, brown; Gd, yellow; O, red; N, blue; Cl, green.

Crystallographic analysis indicated that six ligand anions were participated in the growth of the self-assembled cluster by incorporating six Cu^{II} and three Gd^{III} ions. Among these three were present as HL^- and other three as L^{2-}, each one of them taking care of one Cu^{II} ion within the imine nitrogen bearing ONO pocket I. The hard ether oxygen bearing outer OO chelate bites (pocket II) were used to bind two peripheral Gd^{III} ions. The mineralized core structure was grown over six μ_3-hydroxo and three μ_3-chlorido groups. Within this core, two highly distorted edge sharing open dicubane $[Cu_2Gd_2O_4Cl_2]$ subunits were fused together with a common Gd2 center trapped without any ligand support. Among these subunits the M–X–M angles (M = Cu^{2+}/Gd^{3+}; X = $O^-/OH^-/Cl^-$) range within 80.36°–132.46° showing distortion from the individual ideal angles. For the $[Cu_6Gd_3O_{12}Cl_3]^{6+}$ core, Cu1, Cu2 and Cu3 centers are in the same plane and Cu4, Cu5 and Cu6 centers are in a different parallel plane (Fig. S3 in the ESI).

The in-plane Cu···Cu separations lie within 5.365–5.501 Å, where lower range is accounted for Cu5···Cu6 and higher limit is for Cu4···Cu5. Both the parallel planes incorporating three Cu^{II} centers remain ~4.2 Å apart. All the three Gd^{III} centers are co-linear and co-planer and this unique plane lies vertical to both the Cu^{II} bearing planes (Fig. 2). Each Cu^{II} center lies within slightly distorted square pyramidal NO_3Cl environment. Their trigonality-index values (Addison parameter) τ_5[52] are lies within the range of 0.06–0.12 (τ_5 value 0 is considered for perfect square pyramidal and 1 for TBP geometries, respectively) for all the six Cu^{II} centers. This coordination plasticity is favourable for the growth of *Cu-4f* aggregates under coordination control of bridging and flexidentate multiprotic ligand anions. The SHAPE analysis for all the Cu centers also confirms the square pyramidal environments (Fig. 3; Table S3 in the ESI). In all the six cases, the coordination demand of the Cu^{II} centers is fulfilled by ONO donation from each HL^-/L^{2-} ligand, one μ_3-OH group and one μ_3-chlorido group. The Cu–N distances lies within a wide range of 1.913(9)–1.955(8) Å possibly due to the presence of two types of deprotonated ligand system (HL^- and L^{2-}). The Cu–O bond length lies within 1.912–1.961 Å due to the involvement of four different types of O atoms. For all the six Cu^{II} centers, the μ_3-chlorido donors occupy vertical positions in square-pyramidal geometry with a longer Cu–Cl bonds at 2.774–2.822 Å range.

Within the core structure, each Cu^{II} center forms a highly distorted open cubane subunit involving two neighbouring Gd^{III} centers, one chloride and three O atoms. Within each open-cubane subunits the Cu···Gd separations adjust and cover a wide range of 3.444–3.798 Å. The inter lanthanide distances are very close at ~3.583 Å. The ligand bound Gd^{III} centers, Gd1 and Gd3 are ten coordinated assembled from O,–OMe bidentate donor atoms of three ligands, three μ_3-hydroxo group and one coordinated hydroxo group. The SHAPE 2.1 based analysis of geometry around Gd1 and Gd3 centers confirmed distorted sphenocorona (JSPC-10 = 1.837, Table S5 in the ESI; Fig. S4) structure. The central Gd2 is not bound to any ligand anion donor site, but instead trapped by six μ_3-HO^- and three μ_3-Cl^- groups. From SHAPE 2.1 analysis the nine coordinated environment of Gd2 is confirmed as distorted tricapped trigonal prism with JTCTPR-9 = 0.935 (Table S6 in the ESI; Fig. S4). Four different types of O atoms were gathered around the ligand anion bound Gd^{III} centers and recorded Gd–O distances in 2.400(7)–2.778(8) Å range where Gd3–O10 is the longest one from –OMe binding.

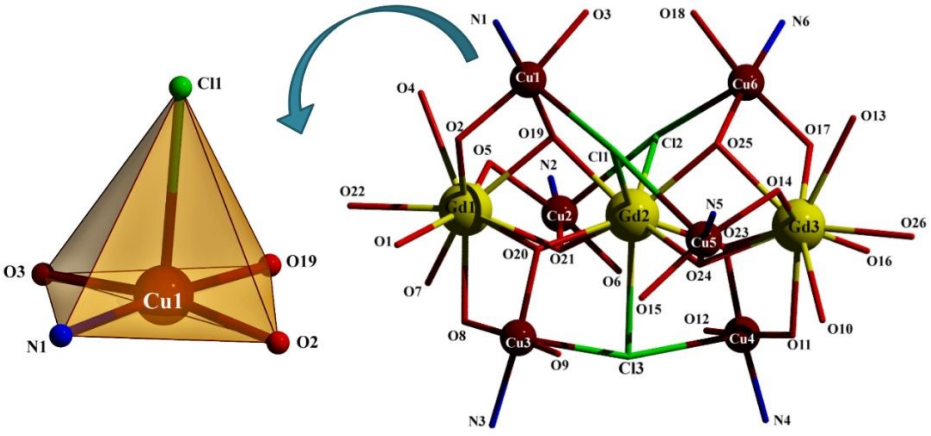

Fig. 3 Core structure of **1** with atom numbering scheme, showing the distorted square pyramidal geometry for Cu1 as a representative center.

For central Gd2 center, the Gd–O and Gd–Cl bonds span the ranges 2.364(7)–2.405(6) Å and 2.997(2)–3.023(3) Å respectively. The Gd–O–Gd angles within $CuGd_2O_3Cl$ open-cubane subunit lie within 95.20(2)–96.50(2)°. The Cu–O–Gd angles, on the other hand are different due to the presence of two types of Gd^{III} centers. Such angles involving terminal Gd centers are narrower in 103.95(3)–106.0(3)° range compared to the those around the central Gd center, where the values span from 120.24(3)–123.05(3)°. The very long Gd–Cl bonds are responsible for narrowing down the Cu–Cl–Gd angles to 80.36(5)–81.29(5)°. There is no strong intramolecular hydrogen bonding interaction for the secondary level stabilization of the metal ion cantered aggregates. Only two weak hydrogen bonding interactions were identified between the alkoxido oxygen of one ligand anion and the alcoholic hydrogen of the adjacent metal ion binding organic scaffold. On the other hand, anion mediated 1D hydrogen bonding network between two Cu_6Gd_3 units through perchlorate counter anion and terminal Gd1···Gd3 bridged hydroxide group provide a chain arrangement (Fig. S5 in the ESI).

Crystal structure description of 2

Block-shaped single crystals of **2** were isolated from the reaction mixture after a week. Initial X-ray crystallographic cell determination revealed that complex **2** crystalized in triclinic P $\bar{1}$ space group. The asymmetric unit consists of $[Cu_3Dy(L)_2(\mu\text{-}Cl)(\mu_3\text{-}OH)_2(H_2O)_3ClO_4]$ unit, two perchlorate anions and two $Et_3NH^+Cl^-$ units within the crystal lattice (Fig. S6 in the ESI). The molecular formula of **2** identified as $[Cu_5Dy_2(L)_2(HL)_2(\mu\text{-}Cl)_2(\mu_3\text{-}OH)_4(H_2O)_6(ClO_4)_2](ClO_4)_2{\cdot}2NHEt_3Cl{\cdot}21H_2O$ (Fig. 4a). The parameters for crystal structure data collection, structure solution and refinement are given in Table S2, and the selected interatomic distances and angles are collected in Tables S10–S11 respectively.

The molecule has an overall center of symmetry where the central Cu3 center resides on a crystallographic inversion center and the whole molecule is generated by rotation around a 2-fold axis. The tetracationic $\{Cu_5Dy_2\}$ cluster is assembled from the use of two L^{2-} and two HL^- anions exhibiting two different connectivity patterns. The structural analysis revealed presence of four ligand anion in two different level of deprotonation serve to hold four peripheral Cu^{II} and two Dy^{III} centers using bridging phenoxido, alkoxido and μ_3-hydroxide groups. L^{2-} parts showed tridentate coordination and bridge Cu···Dy part by terminal alkoxido group, where the –OMe function remained dangling. Whereas the HL^- anion was able to connect the Cu···Dy section through phenoxido bridging and the –OMe coordination. From the bridging action of two hydroxido bridges the formed reaction intermediates were obtained as $[Cu_2Dy(L)(HL)(\mu\text{-}OH)_2]$. Two such intermediates next were able to trap the fifth Cu^{II} center as *in situ* generated $CuCl_2$. The core structure of **2** was grown on a vertex-shared open dicubane $[Cu_3Dy_2O_6Cl_2]$ unit (Fig. 4b). The Cu–O and Dy–O distances for L^{2-} bridges to Cu1, Dy1 and Cu1*, Dy1*, respectively, remained at 1.935(4) Å and 2.219(4) Å. The bridges from HL^- to corresponding Cu^{II} and Dy^{III} centers recorded Cu–O and Dy–O separations of 1.919(4) and 2.316(4) Å. Within this intermetallic core structure two neighboring Cu^{II} centers are separated by 3.256 and 3.337 Å. Within this motif, the $\angle Cu2-O8-Cu3$ angle is wider at 110.79° compared to the $\angle Cu2-Cl1-Cu3$ angle at 74.51°, due to the longer Cu–O bonds. The other Cu–O–Cu ($\angle Cu1-O8-Cu3$) angle is wide at 115.72°.

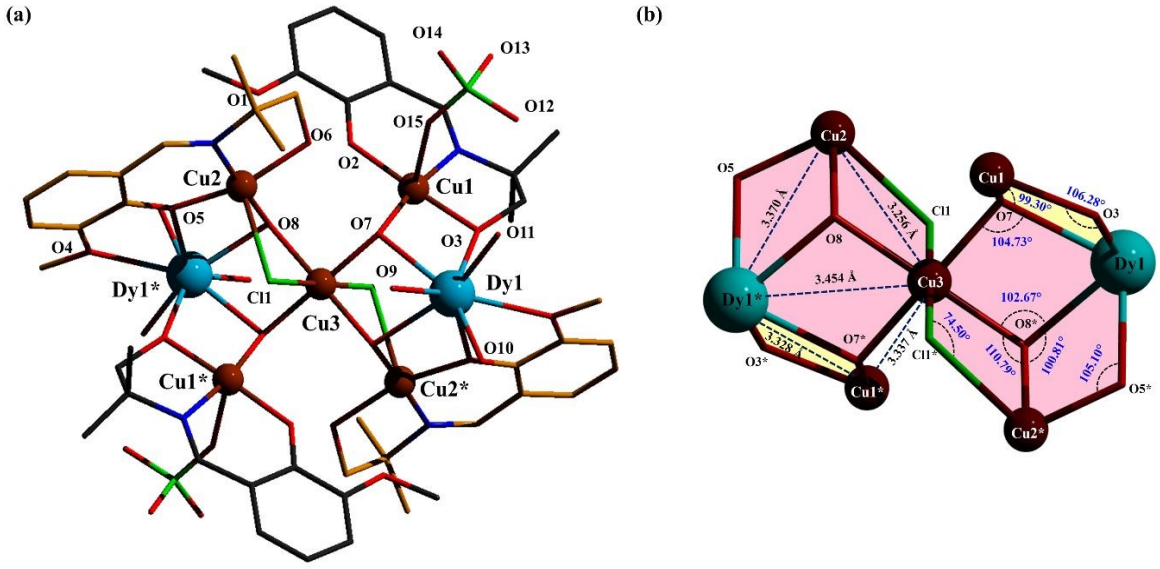

Fig. 4 (a) Molecular structure of **2** with partial atom numbering scheme. H atoms, solvent molecules and counter anions are omitted for clarity. Colour code: Cu, brown; Dy, cyan; C, grey and orange; O, red; N, blue; Cl, green. (b) Core structure of **2** grown on vertex-shared open-dicubane $[Cu_3Dy_2O_6Cl_2]$ and clipping of two other Cu^{II} centers (Cu1 and Cu1*).

View Article Online
DOI: 10.1039/D2DT03932J

The distance of Dy1 from all three Cu centers (Cu1, Cu2 and Cu3) span 3.329–3.454 Å range. Out of the five Cu^{II} centers, the Cu1(Cu1*) centers remained in five-coordinate distorted square pyramidal NO_4 geometry, as indicated by the trigonality-index (Addison parameter[52], τ_5) value of 0.046 (Fig. S7a) whereas Cu2(Cu2*) centers are in NO_3Cl distorted square pyramidal geometries, which gave a τ_5 value of 0.215 (Fig. S7b). Such plasticity in coordination geometry around the Cu1 and Cu2 centers is important for the accommodation of several metal ions in a single entity. The imine nitrogen bonds for four Cu^{II} centers register Cu–N bonds within 1.920(4)–1.931(5) Å range and the Cu–O separations, from different types of oxygen donors, span a wide range from 1.919(4)–2.781(4) Å. The central Cu3 center is trapped with only Cl^- and HO^- supports in an axially elongated Cl_2O_4 octahedral geometry (Fig. S7c, Table S4 in the ESI). The longer Cu–Cl distance of 2.695(3) Å clearly distinguish the Cl–Cu–Cl axis as the axis of elongation having ∠Cl–Cu–Cl angle of 180º. Around the Cu3 center, the Cu–O distances remain within 1.969(4)–2.005(3) Å range and SHAPE 2.1 analysis further confirmed all these observation of different coordination geometry around Cu^{II} centers.

Two Dy^{III} centers (Dy1/Dy1*) in **2** remain in eight-coordinated distorted triangular dodecahedron geometry with TDD-8 = 2.569. (Table S7 in the ESI; Fig. S7d). The Dy–O distances lie within 2.219(4)–2.578(4) Å with longest one is for coordination MeO– group. The Dy···Cu separations remain within 3.328–3.454 Å range. Mean plan analysis revealed that all five Cu centers are within a best plane and Dy1 (or Dy1*) center is 2.392 Å away from this plane, whereas Dy···Dy separation is 6.908 Å. Within the core, several ∠Cu – O – Dy angles were present involving phenoxido, alkoxido and hydroxido linkers and span the range from 99.30°(13) to 105.10(15)°. No characteristic inter-molecular hydrogen bonding interactions were observed. Only intra molecular H-bonding interactions were visible between the PhO^- or RO^- parts of ligand backbone, $NEt_3H^+Cl^-$ and ClO_4^- units and lattice H_2O molecules. The terminal alkoxido oxygen (O2) shows weak hydrogen bonding interaction with the phenoxido oxygen (O6) and the hydroxido oxygen (O7). The O11 of Dy^{III} bound H_2O, functions as hydrogen bond donor to the O12 of lattice ClO_4^- with an average D···A separation of 2.843 Å. The other O atoms of bound H_2O (O9 and O10) forms weak hydrogen bonding interactions with the lattice Cl5 and O25 involved in a hydrogen bonding interaction with the bridging chloride ion Cl1 (Fig. S8, Table S12 in the ESI).

Mass spectral indications in solution

To get a reasonable idea about the nature of the various intermediate fragments present in solution and participate in the self-assembly processes, MeOH solutions of **1** and **2** were examined by ESI-MS (+ve mode). The ESI–MS spectra of **1** and **2** were given in the ESI (Fig. S10–S11). For both the compounds, the identification of the fragments in solution was similar up to the m/z values of 200–600 but the peaks in the latter parts are different probably due to the presence of species having different nuclear types. For both **1** and **2** a base peak at m/z value of 285.1240 corresponds to $[Cu(HL)]^+$ ($C_{12}H_{16}CuNO_3$; calcd 284.04). A medium intensity peak of m/z value 350.4404 was considered for $[Cu(L)(H_2O) + 0.5\ H_2O + K]^+$ ($C_{12}H_{18}CuKNO_{4.5}$; calcd 350.01) fragment and another m/z value of 570.6045 matches well with the Cu_2 species of type $[Cu_2(L)(HL)]^+$ ($C_{24}H_{31}Cu_2N_2O_6$; Calcd. 570.60). These information did suggest that the mono- and dinuclear intermediates do exist in the MeOH solutions of both **1** and **2**, and the $[Cu_2(L)(HL)]^+$ species could attach *4f* ion toward the formation of heteronuclear fragments for the growth of both the assemblies. For complex **1** the highest magnitude of found m/z value of 1174.8397 was due to the presence of $[Cu_6Gd_3(L)_6(OH)_6Cl_2 + H]^{2+}$ ($C_{72}H_{92}Cl_2Cu_6Gd_3N_6O_{24}$; Calcd. 2349.46). On the other hand, for complex **2**, the characteristic m/z value of 962.0592 could be assigned to $[Cu_5Dy_2(L)_4(OH)_4Cl_2(H_2O)_3(ClO_4)_2]^{2+}$ ($C_{48}H_{74}Cl_4Cu_5Dy_2N_4O_{27}$; Calcd. 1923.65).

Magnetic properties

Direct current magnetic susceptibility measurements (dc) for **1** and **2** were performed in the 290-2 K range under a 0.1 Tesla applied magnetic field (Fig. 5). The room temperature $\chi_M T$ values of 26.0 $cm^3\ mol^{-1}$ K and 30.2 $cm^3\ mol^{-1}$ K are close to the theoretical values of 26.1 $cm^3\ mol^{-1}$ K and 30.4 $cm^3\ mol^{-1}$ K for six non-interacting Cu^{II} ions (S=1/2, g = 2.1) and three Gd^{III} ions ($^8S_{7/2}$, S = 7/2, g = 2) and for five non-interacting Cu^{II} ions (S=1/2, g = 2.1) and two Dy^{III} ions ($^6H_{15/2}$, S = 5/2, L = 5, g = 4/3) respectively. For **1**, $\chi_M T$ decreases steadily upon cooling to 23.5 $cm^3\ mol^{-1}$ K at 30 K and then decreases sharply to 8.0 $cm^3\ mol^{-1}$ K at 2 K, indicating dominant antiferromagnetic interactions between the metal ions.[53] For **2**, upon cooling $\chi_M T$ decreases steadily to 26.3 $cm^3\ mol^{-1}$ K at 26 K, before increasing to 45.9 $cm^3\ mol^{-1}$ K at 2 K (Fig. 5). More specifically, for **1**, the Cu···Cu exchange interactions are mediated by μ-Cl groups with the Cu–Cl–Cu angles ranging from 159-162°. This range of Cu–Cl–Cu angles has been reported to promote antiferromagnetic interactions.[53,54] In addition, the Cu···Gd interactions are mediated by (i) μ_3-OH groups with Cu–O–Gd angles in the range of 104–123°, (ii) by μ-O(Ph) groups with the Cu–O–Gd angles found in the range of 104–106° and by (iii) μ-Cl groups with the Cu–Cl–Gd angles found from 80–81°. The Cu–O–Cu angles range from 104–123° and the Cu–O–Gd–O dihedral angles range from 6.6–9.4°. It has been reported that Cu···Gd interactions with obtuse Cu–O–Gd angles and small dihedral Cu–O–Gd–O angles are likely to lead to ferromagnetic exchange interactions.[53] Moreover, the Gd···Gd interactions are mediated by μ_3-OH groups with the Gd–O–Gd angles found in the range of 95.1–96.5°, reported to lead to antiferromagnetic

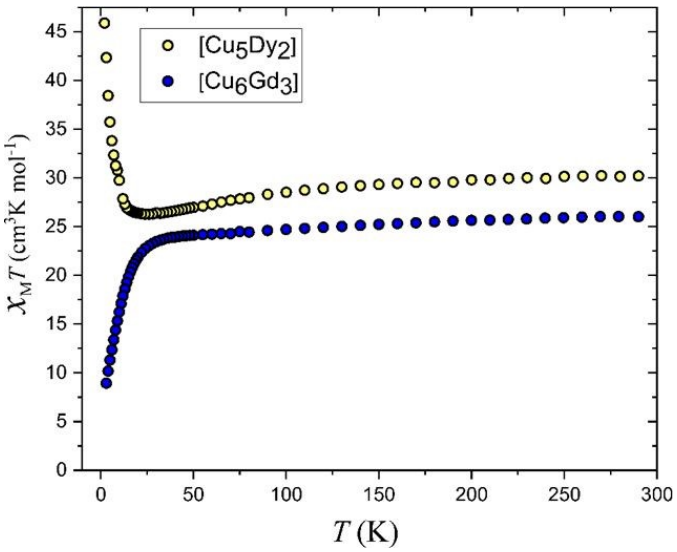

Fig. 5 $\chi_M T$ *vs.* *T* data for **1** and **2** in a field of 1000 Oe from 290 – 2 K.

interactions.[53] Hence, the range of different exchange interactions combined with the large number of metal ions in **1** prevented any attempts to fit the $\chi_M T$ *vs.* *T* data. Additionally, field-dependent magnetisation measurements at 2 K, 4 K and 6 K have been performed for **1** and **2** in the magnetic field range of 0-5 T and 0-7 T, respectively (Fig. S12).

The magnetization plots for **1** (Fig. S12-S13) reach $M/N\mu_B$ = 19.6 at 2 K, which is lower than the maximum value of ~27 $N\mu_B$ (for three Gd^{III} ions and six Cu^{II} ions uncoupled or ferromagnetically coupled) in agreement with the presence of dominant antiferromagnetic interactions. The magnetization plots for **2** (Fig. S12-S13) shows a rapid increase upon increasing the applied field reaching $M/N\mu_B$ = 12.5, 12.3 and 11.9 at 2 K, 4 K and 6 K, respectively. $M/N\mu_B$ at 2 K is lower than the maximum value of ~25 $N\mu_B$ (for two Dy^{III} ions and five Cu^{II} ions uncoupled or ferromagnetically coupled) consistent with the presence of magnetic anisotropy from Dy^{III} and/or a not well-defined ground state with low-lying excited states. Next, we evaluated the magnetothermal properties of **1** by measuring the isothermal magnetization in the temperature range of 2–10 K under an external magnetic field of 0.05–7 T. The magnetic entropy changes, $-\Delta S_m$ were calculated according to the Maxwell relation $-\Delta S_m(T)_{\Delta H} = \int \left[\frac{\partial M(T,H)}{\partial T}\right]_H dH$, giving $-\Delta S_m$ = 11.3 J kg^{-1} K^{-1} at 2 K for ΔH = 7 T (Fig. 6).[55]

Alternating current (ac) susceptibility measurements in the temperature range of 2–6 K under zero applied dc magnetic field and at the frequency range 1.0–1488 Hz were performed in order to study the dynamic magnetic behaviour of **2**. Under zero external dc field, the out-of-phase, χ_M'' susceptibility data show temperature (Fig. 7) and frequency (Fig. 8) dependent peaks. The relaxation times, τ, were extracted from the fits of χ_M'' vs. χ_M' using the generalized Debye model (Fig. 9 left).[56] The α parameters found are in the range of 0.05-0.19 (2–4 K) indicating narrow distribution of relaxation times. The Arrhenius plot, constructed using the relaxation times, τ, is fitted with the Arrhenius equation $\tau = \tau_0 \cdot \exp\left(\frac{U_{eff}}{T}\right)$. The lnτ *vs.* 1/T plot is fitted considering an Orbach process, yielding an energy barrier of U_{eff} = 15.8 K and τ_0 = 9.8 x 10^{-7} s (Fig. 9 right).

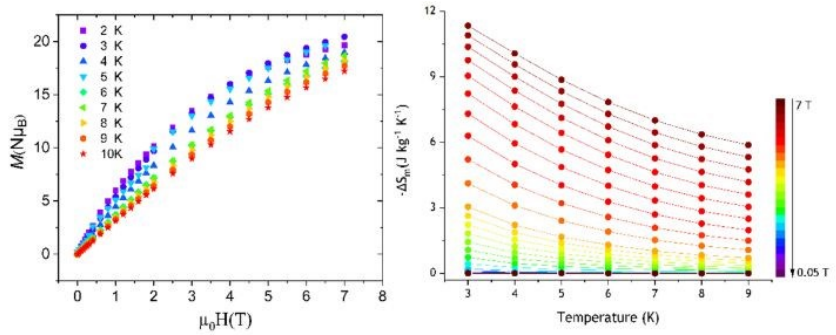

Fig. 6 (Left) Magnetisation *vs.* Field plots for **1** in the temperature range 2-10 K. (Right) $-\Delta S_m$ values for **1**, calculated from the Maxwell equation.

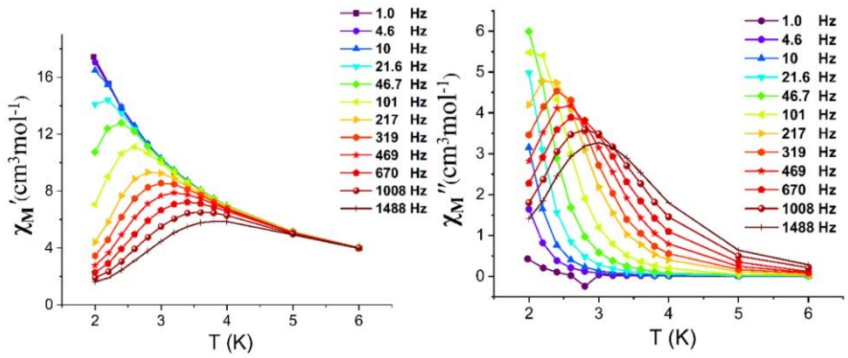

Fig. 7 Temperature dependence of the in-phase, χ'_M (left), and out-of-phase, χ''_M (right) ac susceptibility, in zero dc field, for **2** with ac frequencies of 1.0–1488 Hz.

View Article Online
DOI: 10.1039/D2DT03932J

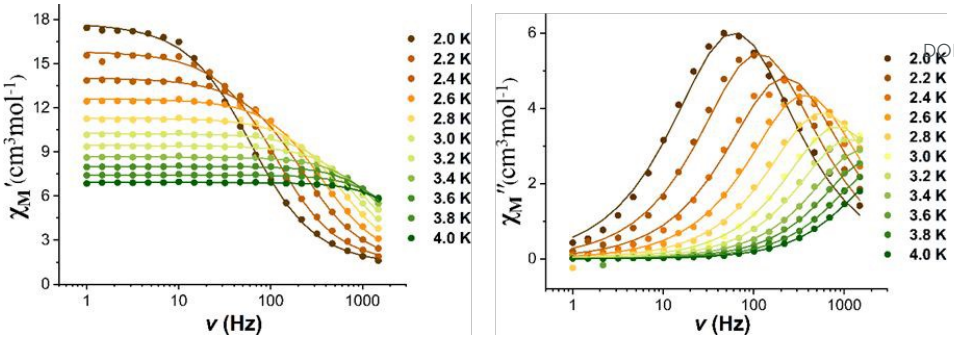

Fig. 8 Frequency dependence of the in-phase χ'_M (left), and out-of-phase, χ''_M (right) ac susceptibility for **2** up to 4 K in zero dc field. The solid lines correspond to the best fit to Debye's law.

Cancer Cell Growth Inhibition by 1 and 2

Increased availability of new family of lanthanide compounds with higher level of stability has made new promises which led to the screening of these complexes in the applications in cancer therapy.[57] Complexes of Ln^{III} ions are known to be active against several cancer cell lines.[58] It is now well known that DNA is the primary target for this purpose which is based on the formation of DNA adducts with therapeutically active metal ion complexes.[59] Mutations within DNA play a substantial role in the development of tumours. The cleavage of DNA via ligand anion bound lanthanide(III) fragments are important to understand the unidentified mutations that lead to the growth of cancer state and thus the new proposals for the modus operandi for the treatment of this disease using metal ions were gaining ground. As a consequence of the abundance of negatively charged and hard oxygen donor groups, the DNA polyelectrolyte readily interacts with compatible hard lanthanide(III) ions and may be anticipated to occupy at least some of the inner-sphere coordination sites of the cations by replacing bound water molecules. The metal ion complexes used as anticancer agents can bind to carrier proteins in the blood.[60] In particular, some lanthanide complexes of Ce^{III}, Er^{III}, Pr^{III}, Yb^{III}, Gd^{III} etc. with Schiff bases are known to be bioactive.[61–63]

In order to test the cytotoxic efficiency across different cancer types, we tested the cytotoxic property of the synthesized *3d-4f* compounds **1** and **2** against cell lines derived from human lung (A549) and breast cancer (MD-MB-231) by MTT assay. MTT assay determines the cytotoxicity of any compound on the basis of the activity of mitochondrial dehydrogenase enzyme present in the cells.[64] Reproducible IC_{50} values were obtained for all the complexes and are given in Table 1. Appropriate metal precursors such as $Cu(ClO_4)_2 \cdot 6H_2O$, $DyCl_3 \cdot 6H_2O$, $GdCl_3 \cdot 6H_2O$ and the ligand (H_2L) used in the synthesis of the complexes were also tested for cytotoxicity and found to be poor inhibitors of cancer cell growth (Fig. S14–S17). Herein we found that the coordination of the Schiff base ligand to *3d* and *4f* metal ions, enhanced the cytotoxicity of these **1** (**Gd**) and **2** (**Dy**) relative to their metal ion precursors against both the cancer cell lines. Amongst the complexes examined, significant increment in cytotoxic behaviour was observed for **1** (Fig. 10).

To determine if the growth inhibitory effect of the complexes is specific to cancer cells; HEK293T cells, which are normal human embryonic kidney cell line were used for cytotoxicity experiments. HEK293T cells are relatively resistant to **1** and **2** compared to other cancer cell lines. Comparable IC_{50} values for these complexes against MD-MB-231 and HEK293T cell lines suggest that both **1** and **2** are selectively active against A549 cells. Thus, we conclude that both the synthesized complexes **1** and **2** are specifically cytotoxic to lung cancer cell lines. Furthermore, among the two synthesized complexes, complex **1** is found to be the most cytotoxic against A549 human lung cancer cells (IC_{50} 4.76 ± 0.02 μM) selectively.

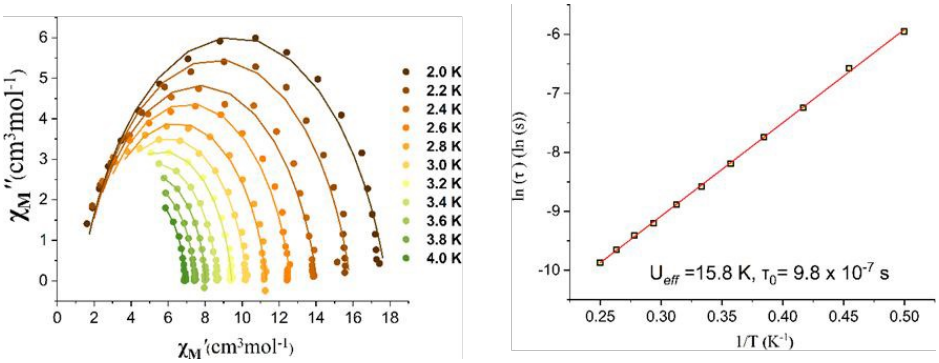

Fig. 9 (Left) χ''_M vs. χ'_M plot of the ac magnetic susceptibility of **2** in zero dc field. The solid lines correspond to the best fit to Debye's law; (Right) Plot of the relaxation time τ (logarithmic scale) versus T^{-1}. The solid red line represents the best fit to the Arrhenius law.

View Article Online
DOI: 10.1039/D2DT03873J

Interactions of 1 and 2 with DNA

DNA is one of the prime targets for several anticancer active compounds including several metal ion complexes.[65–67] In order to investigate the interactions of these complexes with DNA, various biophysical experiments like ethidium bromide displacement assay and electronic spectral studies were performed. The results obtained from these experiments are summarized below and reported in detail in the ESI. In case of UV-vis absorption titrations study, unlike classical intercalator like ethidium bromide (EB), moderate hypochromic effect with minor red shift in the absorption band of **1** and **2** has been observed (Fig. S18). The association constant (K_a) has been calculated following the Benesi–Hildebrand approach using equation S1 as defined in the ESI. The intrinsic binding constant (K_a) values of **1** and **2** were found to be 9.8(± 0.26) x 10^3 M^{-1} and 48.5(± 0.12) x 10^3 M^{-1}, respectively. Thus, the observed order for the DNA binding propensity is **2** > **1** (Table 2). However, the binding constant values are much smaller compared to EB intercalator (EB-DNA, 1.4 × 10^6 M^{-1}), which ruled out the possibility of strong intercalation.[68] However, the nonexistence of any isosbestic point in the absorption spectra upon addition of DNA further implies that 1:1, complex: DNA stoichiometry is probably not maintained during the binding process and hence, more than one type of binding of these fragments with DNA cannot be ruled out. In order to obtain further insight into the nature of interactions of the complexes with DNA, relative binding affinity of **1** and **2** for *ct*-DNA has been studied by fluorometric titration using EB as an optical probe (Fig. S19 in the ESI). The K_{sv} values obtained using the Stern–Volmer equation (S2) for **1** and **2** are in the range of 8.85 and 11.6 × 10^4 M^{-1} respectively (Table 3). This result clearly shows that complex **2** can substitute EB more effectively compared to **1**. The binding proficiency of the compounds can be compared with the classical intercalator EB by calculating the apparent binding constants (K_{app}) from eqn S3 in the ESI. The apparent binding constants for complexes **1** and **2** are smaller than the binding constant of EB (1 × 10^7 M^{-1}). However, the DNA binding order observed from this study shows similar trend as obtained from the UV–Vis spectral study. Therefore, from the observed quenching and binding studies using electronic spectral measurements it may be concluded that both the complexes bind *ct*–DNA *via* groove binding as the strength of binding constants are not comparable with the standard intercalator.

HSA binding studies

Human serum albumin (HSA) is the major constituent of blood plasma which plays crucial roles in transportation of drug molecules, their storage and metabolism. Interaction of **1** and **2** with HSA protein had been studied using quenching of intrinsic tryptophan fluorescence of HSA. Intrinsic fluorescence of HSA is due to the presence of tryptophan residues (Trp-214) in a hydrophobic environment. The fluorescence intensity of HSA centered at 347 nm decreases steadily with gradual increase of concentration of **1** and **2**.

Table 1 IC_{50} values of the complexes and starting precursors against cancerous and non-cancerous cell lines

	IC_{50}[a] in (μM)		
	A549	**MD-MB-231**	**HEK293T**
Compound **1**	4.76 ± 0.02	18.48 ± 0.03	31.16 ± 0.04
Compound **2**	22.09 ± 0.03	35.97 ± 0.01	37.41 ± 0.05
$Cu(ClO_4)_2{\cdot}6H_2O$	41.79 ± 0.04	78.31 ± 0.23	58.97 ± 0.02
$DyCl_3{\cdot}6H_2O$	59.37 ± 0.02	29.2 ± 0.09	41.60 ± 0.23
$GdCl_3{\cdot}6H_2O$	47.1 ± 0.05	23.95 ± 0.001	27.59 ± 0.06
H_2L	36.88 ± 0.75	47.73 ± 0.02	58.84 ± 0.06

a. values are in triplicate

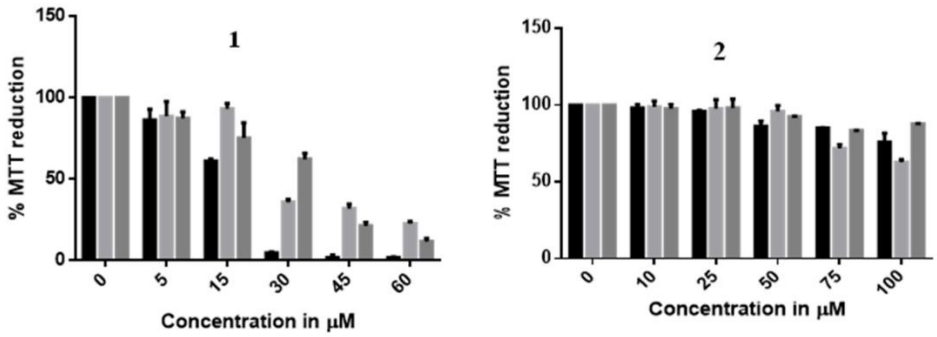

Fig. 10 Percentage of cell growth as a function of concentration of **1** and **2** for A549 (black bars), MDA-MB231 (light grey bars) and HEK293T (dark grey bars) cell lines. The experimental number of cells counted was normalized so that the average of all control experiments was considered as 100%. At least three independent experiments were performed on different days.

Table 2. Association constants (K_a) for the interaction of *ct*-DNA (0–50 μM) with **1** and **2** (25μM) at 298 K

System	K_a[b] (L mol^{-1})
***ct*-DNA-1**	9.8 (± 0.26) × 10^3
***ct*-DNA-2**	48.5 (± 0.12) × 10^3

b. values are in triplicate

Table 3. Stern-volmer quenching constant and apparent binding constant of the studied compounds

System	K_{SV} (L M^{-1})	R^2	K_{app}
***ct*-DNA-1**	8.85 × 10^4	0.97901	15.6 × 10^4
***ct*-DNA-2**	11.6 × 10^4	0.97178	22.3 × 10^4

The significant quenching of emission intensity possibly results from various molecular interactions arises due to perturbation of HSA secondary structure upon binding of the lanthanide complexes including subunit association, substrate binding of the protein. The Stern-Volmer quenching constant for HSA fluorescence (K_{SV}) for **1** and **2** have been calculated from equation S4 and corresponding plots from the slope of the linear portion in the regression curve (Fig. S20, see ESI). The bimolecular quenching constants (k_q) were calculated using eqn S5 of the ESI. Further, the quenching constant, also known as the binding constant K_a, and the number of binding sites (n) between the protein and metal complexes were calculated using the Scatchard equation S6. The values of K_{SV} and n for complexes **1** and **2** are summarized in Table 4.

The K_a values of ~10^4 M^{-1} indicate that the complexes favorably bind to serum proteins thus possibly may enhances the transport and release of protein-bound complexes through biological fluids at cellular level. The k_q values (~10^{14}) of **1** and **2** (Table 4) are higher than the limiting diffusion constants (K_{dif} = 2.0 × 10^{10} M^{-1} s^{-1}) of the biomolecules.[69] This indicates that static quenching is predominant in these systems.[70–72] Considerable size of the complexes and fragments are distinctive in quenching the fluorescence of Trp in HSA *via* thermodynamically favourable interactions with high binding constant values. The fluorescence quenching by **1** is the greatest in this group (Table S13, 60.2%). The binding constants of the complexes follow the order **1** > **2** as presented in Table 4. Higher affinity of **1** to HSA than **2** is possibly due to better hydrophobic interactions with amino acid probe residues. Direct relationship between the binding constant values and the number of binding sites has been shown in Table 4. The values of *n* are near 1 which indicates the presence of single affinity binding site in HSA for both the compounds. It is quite noteworthy that K_a values obtained for both the compounds are in accordance being within an optimum range; i.e., they are high enough to allow the binding of the compounds to HSA which facilitates their transfer and their binding constants are much below than the association constant of one of the strongest known non-covalent bonds (the interaction of avidin with diverse ligands with a K_a value ≈ 10^{15} M^{-1}). These suggests a possible release from the serum albumin to the target cells.[73–75]

Table 4. Summary of the Stern–Volmer constant; K_{sv}, quenching constant; k_q, binding constant; K_a, and number of binding sites; *n*, for the interactions of **1**–**2** with HAS

System	K_{SV} (L mol^{-1})	k_q (L mol^{-1} s^{-1})	K_a (L mol^{-1})	*n*
HSA-1	2.19 × 10^5	4.38 × 10^{13}	3.998 × 10^4	1.0
HSA-2	1.06 × 10^5	2.12 × 10^{13}	2.70 × 10^4	1.4

Conclusions

Synergistic metal ion coordination induced self-assembly in reaction medium finally resulted two different types of aggregates depending upon the nature of the lanthanide ions. Competitive binding and bridging of central phenoxido and terminal alkoxido groups of the ligand scaffold dictate the mode of assembly processes around the lanthanide ions. Thus reactivity of ligand anions HL^- and L^{2-} for $Cu(ClO_4)_2{\cdot}6H_2O$ and $LnCl_3{\cdot}5H_2O$ (Gd^{III} and Dy^{III}) salts, resulted two structurally contrasting and functionally different coordination aggregates **1** (Cu_6Gd_3) and **2** (Cu_5Dy_2). Presence of NEt_3 as base in MeOH-$CHCl_3$ (2:1) reaction medium was crucial to provided required amount of *in situ* generated HO^- ions for mineral like growth for the *3d-4f* cores. Further, *in situ* available Cl^- directed two distinct reaction paths by capturing $GdCl_3$ and $CuCl_2$ as two different nucleating centers for the growth of the aggregates. Compound **1** showed magnetic coolant properties in solid state. Analysis of the magnetothermal data for **1** gives $-\Delta S_m$ = 11.3 J kg^{-1} K^{-1} at 2 K for ΔH = 7 T. In contrast, **2** shows slow magnetic relaxation typical of single-molecule magnets. The ac susceptibility measurements of **2** in the 2–6 K temperature range under zero applied dc magnetic field show temperature and frequency dependence. Analysis of this data gives an energy barrier of U_{eff} = 15.8 K and τ_0 = 9.8 x 10^{-7} s.

In terms of solution level activity in the biological media, we identified that both **1** and **2** to function as inhibitors for cancer cell line growths and interestingly the Cu_6Gd_3 compound found to be the most active against A549 cell lines. Both the compounds showed interactions with DNA in groove binding mode. UV-vis and fluorescence spectral measurements indicated that the association followed the order **2** > **1**. Furthermore, affinity of **1** and **2** for HSA had been studied in order to appreciate the carrier role of serum albumin towards the DNA targets. These findings should be valuable in understanding the relationship of DNA–binding behaviours of *3d-4f* complexes and usage of Gd based compounds as cytotoxic agents against cancer cell lines laying a foundation for the rational design of novel, powerful agents for probing and targeting nucleic acids and proteins.

Conflicts of interest

The authors declare no conflict of interest.

Acknowledgements

AB is thankful to DST-INSPIRE for the research fellowship and for the single-crystal XRD facility at the Department of Chemistry, IIT Kharagpur, we acknowledge the FIST program of DST, New Delhi. We are also thankful to Prof. Swagata Dasgupta of Department of Chemistry, IIT Kharagpur, India, for allowing us to study the biological interactions of our compounds in her lab. SRC is thankful to IIT Kharagpur for the postdoctoral funding. MM thanks the University of Glasgow for financial support and Dr. Marco Evangelisti (Universidad de Zaragoza) for assistance with the MCE data analysis of **1**.

References

1 H. L. C. Feltham and S. Brooker, *Coord. Chem. Rev*., 2014, **276**, 1–33.
2 S. Liu, Y. Gil, C. Zhao, J. Wu, Z. Zhu, X.-L. Li, D. Aravena and J. Tang, *Inorg. Chem. Front*., 2022, **9**, 4982–4989.
3 D. I. Alexandropoulos, L. Cunha-Silva, J. Tang and T. C. Stamatatos, *Dalton Trans*., 2018, **47**, 11934–11941.
4 D. I. Alexandropoulos, L. Cunha-Silva, G. Lorusso, M. Evangelisti, J. Tang and T. C. Stamatatos, *Chem. Commun*., 2016, **52**, 1693–1696.
5 X. Feng, J. Liu, T. D. Harris, S. Hill and J. R. Long, *J. Am. Chem. Soc*., 2012, **134**, 7521–7529.
6 S.-D. Jiang, B.-W. Wang, G. Su, Z.-M. Wang and S. Gao, *Angew. Chem. Int. Ed*., 2010, **49**, 7448 –7451.
7 F. Troiani and M.Affronte, *Chem. Soc. Rev*., 2011, **40**, 3119–3129.
8 G. Aromi, D. Aguila, P. Gamez, F. Luis and O. Roubeau, *Chem. Soc. Rev*., 2012, **41**, 537–546.
9 W. Wernsdorfer, *Nat. Nanotechnol*., 2009, **4**, 145–146.
10 F. Habib and M. Murugesu, *Chem. Soc. Rev*., 2013, **42**, 3278–3288.
11 P. Kumar, J. F. Gonzalez, P. P. Sahu, N. Ahmed, J. Acharya, V. Kumar, O. Cador, F. Pointillart, S. K. Singh and V. Chandrasekhar, *Inorg. Chem. Front*., 2022, **9**, 5072–5092.
12 D. N. Woodruff, R. E. P. Winpenny and R. A. Layfield, *Chem. Rev*., 2013, **113**, 5110–5148.
13 R. Layfield and M. Murugesu, Lanthanides and actinides in molecular magnetism; Wiley-VCH: Weinheim, Germany, 2015.
14 R. Sessoli and A. K. Powell, *Coord. Chem. Rev*., 2009, **253**, 2328–2341.
15 E. C. Mazarakioti, J. Regier, L. Cunha-Silva, W. Wernsdorfer, M. Pilkington, J. Tang and T. C. Stamatatos, *Inorg. Chem*., 2017, **56**, 3568–3578.
16 K. C. Mondal, G. E. Kostakis, Y. Lan, W. Wernsdorfer, C. E. Anson, A. K. Powell, *Inorg. Chem*., 2011, **50**, 11604–11611.
17 G. Novitchi, W. Wernsdorfer, L. F. Chibotaru, J.-P. Costes, C. E. Anson and A. K. Powell, *Angew. Chem. Int. Ed*., 2009, **48**, 1614 –1619.
18 L. Jiang, B. Liu, H.-W. Zhao, J.-L. Tian, X. Liu, S.-P. Yan, *CrystEngComm*., 2017, **19**, 1816–1830.
19 A. B. Canaj, D. I. Tzimopoulos, M. Otręba, T. Lis, R. Inglis and C. J. Milios, *Dalton Trans*., 2015, **44**, 19880–19885.
20 O. Iasco, G. Novitchi, E. Jeanneau and D. Luneau, *Inorg. Chem*., 2013, **52**, 8723–8731.
21 A. Worrell, D. Sun, J. Mayans, C. Lampropoulos, A. Escuer and T. C. Stamatatos, *Inorg. Chem*., 2018, **57**, 13944–13952.
22 J.-D. Leng, J.-L. Liu and M.-L. Tong, *Chem. Commun*., 2012, **48**, 5286–5288.
23 S. Xiang, S. Hu, T. Sheng, R. Fu, X. Wu and X. A. Zhang, *J. Am. Chem. Soc*., 2007, **129**, 15144–15146.
24 C. Aronica, G. Pilet, G. Chastanet, W. Wernsdorfer, J.-F. Jacquot and D. Luneau, *Angew. Chem. Int. Ed*., 2006, **45**, 4659–4662.
25 J. F. Gonzalez, F. Pointillart and O. Cador, *Inorg. Chem. Front*., 2019, **6**, 1081–1086.
26 Z. Zhu, C. Zhao, T. Feng, X. Liu, X. Ying, X.-L. Li, Y.-Q. Zhang and J. Tang, *J. Am. Chem. Soc*., 2021, **143**, 10077–10082.
27 A. B. Canaj, S. Dey, E. R. Marti, C. Wilson, G. Rajaraman and M. Murrie, *Angew. Chem. Int. Ed*., 2019, **58**, 14146 –14151.
28 A. B. Canaj, S. Dey, O. Cespedes, C. Wilson, G. Rajaraman and M. Murrie, *Chem. Commun*., 2020, **56**, 1533–1536.
29 A. B. Canaj, S. Day, C. Wilson, O. Cespedes, G. Rajaraman and M. Murrie, *Chem. Commun*., 2020, **56**, 12037–12040.
30 J. Bartolome, F. Luis and J. F. Fernandez, Molecular magnets: physics and applications. Springer: Berlin, 2014, 365–387.
31 M. Evangelisti, F. Luis, L. J. de Jongh and M. J. Affronte, *J. Mater. Chem*., 2006, **16**, 2534–2549.
32 Jr. J. A. Cotruvo, *ACS Cent. Sci*., 2019, **5**, 1496–1506.
33 Y. He, A. Lopez, Z. Zhang, D. Chen, R. Yang and J. Liu, J. *Coord. Chem. Rev*., 2019, **387**, 235–248.
34 W.-L. Kwong, R. W.-Y. Sun, C.-N. Lok, F.-M. Siu, S.-Y. Wong, K.-H. Low, C.-M. Che, *Chem. Sci*., 2013, **4**, 747–754.
35 A. Walcourt, M. Loyevsky, D. B. Lovejoy, V. R. Gordeuk and D. R. Richardson, *Int. J. Biochem. Cell Biol*., 2004, **36**, 401–407.
36 K. Das, S. Nandi, S. Mondal, T. Askun, Z. Canturk, P. Celikboyun and T. Akitsu, *New J. Chem*., 2015, **39**, 1101–1114.
37 E. Ramachandran, V. Gandin, R. Bertani, P. Sgarbossa, K. Natarajan, N. S. P. Bhuvanesh, A. Venzo, A. Zoleo, A. Glisenti, A. Dolmella, A. Albinati and C. Marzano, *J. Inorg. Biochem*., 2018, **182**, 18–28.
38 X.-Q. Song, Z.-G. Wang, Y. Wang, Y.-Y. Huang and Y.-X. Sun, *J. Biomol. Struct*., 2020, **38**, 733–743.
39 V. F. S. Pape, S. Toth, A. Furedi, K. Szebenyi, A. Lovrics, P. Szabo and G. Szakacsa, *Eur. J. Med. Chem*., 2016, **117**, 335–354.
40 A. Bhanja, E. Moreno-Pineda, R. Herchel, W. Wernsdorfer and D. Ray, *Dalton Trans*., 2020, **49**, 7968–7976.
41 M. Biswas, E. C. Sañudo and D. Ray, *Chem. Asian. J*., 2020, **15**, 2731–2741.
42 A. Bhanja, M. Schulze, R. Herchel, E. Moreno-Pineda, W. Wernsdorfer and D. Ray, *Inorg. Chem*., 2020, **59**, 17929–17944.
43 A. Bhanja, R. Herchel, E. Moreno-Pineda, A. Khara, W. Wernsdorfer and D. Ray, *Dalton Trans*., 2021, **50**, 12517–12527.
44 M. Pait, M. Shatruk and D. Ray, *Dalton Trans*., 2015, **44**, 11741–11754.
45 J. W. Sharples and D. Collison, *Coord. Chem. Rev*., 2014, **260**, 1–20.
46 M. Pait, A. Bauzá, A. Frontera, E. Colacio and D. Ray, *Inorg. Chem*., 2015, **54**, 4709–4723.
47 K. Chattopadhyay, G. A. Craig, M. J. H. Ojea, M. Pait, A. Kundu, J. Lee, M. Murrie, A. Frontera, D. Ray, *Inorg. Chem*., 2017, **56**, 2639–2652.
48 H. Oshio, Y. Saito and T. Ito, *Angew. Chem. Int. Ed. Engl*., 1997, **36**, 2673–2675.
49 M. Dey, C. P. Rao, P. K. Saarenketo and K. Rissanen, *Inorg. Chem. Commun*., 2002, **5**, 380–383.
50 A. Paul, H. Puschmann and S. C. Manna, *Polyhedron*, 2018, **155**, 447–456.
51 K. Nakamoto, Infrared and raman spectra of inorganic and coordination compounds, 4th ed., Wiley: New York, 1986.
52 W. A. Addison, T. N. Rao, J. Reedijk, J. V. Rijn and G. C. J. Verschoor, *J. Chem. Soc. Dalton Trans*., 1984, 1349–1356.
53 T. Rajeshkumar, H. V. Annadata, M. Evangelisti, S. K. Langley, N. F. Chilton, K. S. Murray, G. Rajaraman, *Inorg. Chem*., 2015, **54**, 1661–1670.

54 V. Chandrasekhar, A. Dey, S. Das, M. Rouzieres and R. Clerac, *Inorg. Chem*., 2013, **52**, 2588−2598.
55 M. Evangelisti and E. K. Brechin, *Dalton Trans*., 2010, **39**, 4672−4676.
56 D. Gatteschi, R. Sessoli and J. Villain, Molecular nanomagnets, Oxford University Press, 2006.
57 J.-H. Wei, Z.-F. Chen, J.-L. Qin, Y.-C. Liu, Z.-Q. Li, T.- M. Khan, M. Wang, Y.-H. Jiang, W.-Y. Shen and H. Liang, *Dalton Trans*., 2015, **44**, 11408−11419.
58 R. D. Teo, J. Termini, H. B. Gray, *J. Med. Chem*., 2016, **59**, 6012–6024.
59 K. Karami, Z. M. Lighvan, H. Farrokhpour, M. D. Jahromi and A. A. Momtazi-Borojeni, *J. Biomol. Struct. Dyn*., 2018, **36**, 3324–3340.
60 A. D. Almeida, B. L. Oliveira, J. D. G. Correia, G. Soveral, and A. Casini, *Coord. Chem. Rev*., 2013, **257**, 2689–2704.
61 K. Andiappan, A. Sanmugam, E. Deivanayagam, K. Karuppasamy, H.-S. Kim and D. Vikraman, *Sci. Rep*., 2018, *8*:3054.
62 Y.-H. Fan, A.-D. Wang, C.-F. Bi, Y. Xiao, S.-Y. Bi, X. Zhang, Q. Wang, *Synth. Met*., 2011, **161**, 1552–1556.
63 A. T. Chaviara, P. C. Christidis, A. Papageorgiou, E. Chrysogelou, D. Hadjipavlou-Litina and C. Bolos, *J. Inorg. Biochem*., 2005, **99**, 2102–2109.
64 P. Kumar, S. Senthamilselvi, M. Govindaraju and R. Sankar, *RSC Advances*, 2014, **4**, 46157–46163.

View Article Online DOI: 10.1039/D2DT03932J

65 A. C. Komor and J. K. Barton, *Chem. Commun*., 2013, **49**, 3617–3630.
66 L. H. Hurley, *Nat. Rev. Cancer*, 2002,188–200.
67 K. E. Erkkila, D.T. Odom and J. K. Barton, *Chem. Rev*., 1999, **99**, 2777–2796.
68 J. B. LePecq and C. C. Paoletti, *J. Mol. Biol*., 1967, **27**, 87–106.
69 M. R. Eftink, Fluorescence quenching reaction: probing biological macromolecular structures, biophysical and biochemical aspects of fluorescence spectroscopy, Plenum Press, New York, 1991.
70 C. Harford and B. Sarkar, *Acc. Chem. Res*., 1997, **30**, 123–130.
71 X.-B. Fu, D.-D. Liu, Y. Lin, W. Hu, Z.-W. Mao and X.-Y. Le, *Dalton Trans*., 2014, **43**, 8721–8737.
72 C.-Y. Gao, X. Qiao, Z.-Y. Ma, Z.-G. Wang, J. Lu, J.-L. Tian, J.-Y. Xu and S.-P. Yan, *Dalton Trans*., 2012, **41**, 12220–1223.
73 S. Y. Shi, Y. P. Zhang, X. Q. Chen and M. J. Peng, *J. Agric. Food Chem*., 2011, **59**, 10761–10769.
74 X. W. Li, Y. T. Li, Z. Y. Wu and C. W. Yan, *Inorg. Chim. Acta*, 2012, **390**, 190–198.
75 O. H. Laitinen, V. P. Hytonen, H. R. Nordlund and M. S. Kulomaa, *Cell Mol. Life Sci*., 2006, **63**, 2992–301.